PCCP

ROYAL SOCIETY OF CHEMISTRY

PAPER

View Article Online
View Journal | View Issue

Cite this: *Phys. Chem. Chem. Phys.*, 2024, **26**, 14607

Regulation of π–π interactions between single aromatic molecules by bias voltage†

Xiaona Xu,[a] Keqiang Jia,[a] Qiang Qi,[b] Guangjun Tian *[b] and Dong Xiang *[a]

Received 27th March 2024,
Accepted 29th April 2024

DOI: 10.1039/d4cp01277a

rsc.li/pccp

π-stacking interaction, as a fundamental type of intermolecular interaction, plays a crucial role in generating new functional molecules, altering the optoelectronic properties of materials, and maintaining protein structural stability. However, regulating intermolecular π–π interactions at the single-molecule level without altering the molecular conformation as well as the chemical properties remains a significant challenge. To this end, *via* conductance measurement with thousands of single molecular junctions employing a series of aromatic molecules, we demonstrate that the π–π coupling between neighboring aromatic molecules with rigid structures in a circuit can be greatly enhanced by increasing the bias voltage. We further reveal that this universal regulating effect of bias voltage without molecular conformational variation originates from the increases of the molecular dipole upon an applied electric field. These findings not only supply a non-destructive method to regulate the intermolecular interactions offering an approach to modulate the electron transport through a single molecular junction, but also deepen the understanding of the mechanism of π–π interactions.

Introduction

π–π coupling, as one of the key important intermolecular interactions between aromatic components, has a significant impact on the molecular structure, properties, and functions. The π–π interaction between molecules has been extensively explored in various research fields,[1–4] including supramolecular chemistry,[5–7] molecular biology,[8] organic chemistry,[9–11] and materials science.[12–14] In particular, π–π stacking, as a non-covalent interaction between molecules,[15] significantly influences charge transfer between molecular fragments, which is a critical process in chemistry and biology.[4,8,16] The charge transfer through the molecular dimer junctions formed *via* π–π coupling may determine the performance of molecular-based devices.[17]

Due to the extensive impact of π–π stacking interactions across diverse fields, the effective control of these interactions at the single-molecule level has garnered intensive attention. Different strategies have been put forward to regulate intermolecular interaction so far. It has been demonstrated that π–π interactions between molecules can be manipulated by adjusting the molecular concentration,[18] mechanical modulation,[16,19–21] and molecule design.[22,23] Recently, it was reported that π–π coupling could be regulated *via* molecular conformational changes triggered by an external electric field.[24] Supported by DFT calculations, the authors demonstrated that the molecules become more planar in response to the electric field, leading to the energetically preferred π–π stacking configuration. This finding provides a novel approach to tune molecular assembly using an electric field. However, regulating π–π interaction by such a strategy is limited by the requirement of conformational changes. Here, we further investigated the π–π stacking with a series of rigid and already-planar molecules that are not likely to undergo significant geometrical changes under a bias voltage. Interestingly, the enhancement of π–π stacking is universally observed under a higher bias voltage. Based on these observations, we proposed a more general mechanism for the observation, *i.e.*, increased dipole moments of the molecules and the ordered alignment of molecules upon a higher DC bias voltage result in the enhancement of π–π stacking.

Methods

Conductance measurements

We utilized the scanning tunnelling microscope break junction (STM-BJ) technique to investigate the effect of electric fields on π–π interactions due to its advantages: it can generate a substantial electric field up to 10^9 V m^{-1} by applying a small

[a] *Center of Single-Molecule Sciences, Institute of Modern Optics, Tianjin Key Laboratory of Micro-scale Optical Information Science and Technology, Nankai University, Tianjin 300350, China. E-mail: xiangdongde@nankai.edu.cn*
[b] *State Key Laboratory of Metastable Materials Science & Technology and Key Laboratory for Microstructural Material Physics of Hebei Province, School of Science, Yanshan University, Qinhuangdao, 066004, China. E-mail: tian@ysu.edu.cn*

† Electronic supplementary information (ESI) available. See DOI: https://doi.org/10.1039/d4cp01277a

voltage between the source and drain electrodes;[25] (2) the size of the electrode gap can be flexibly adjusted to form thousands of molecular junctions, and thus the statistical conductance of these junctions can be measured, offering a practical approach to characterize the π–π interactions between neighbouring molecules.[26,27] The experiments were conducted in a solution containing 0.1 mM of the target molecule at room temperature and atmospheric conditions. A gold substrate was prepared using plasma beam sputtering by depositing a 15/200 nm Cr/Au bilayer onto a silicon wafer coated with a 300 nm layer of silicon dioxide. Prior to the experiment, the gold substrate was thoroughly cleaned with an ethanol solution. Gold beads were created by flame cleaning and annealing the gold tip, which had a purity level of 99.999%. Controlled contact between the gold tip and substrate was achieved using piezoelectric ceramics, ensuring reliable and repeatable interactions. More than 3000 individual conductance-displacement traces were collected and subsequently utilized to construct each conductance histogram.

Flicker noise measurement and correlation analysis

For flicker noise spectrum measurements, as previously reported,[28,29] when a low conductivity platform (conductance range from $10^{-4.2}$ G_0 to $10^{-4.9}$ G_0) is observed, the needle tip is hovered for 150 ms during the stretching process between the needle tip and the substrate, and the conductivity time (G–t) trajectory is recorded during the electrode hovering process. The noise spectrum is derived by performing a fast Fourier transform on each G–t curve, and then the noise power is obtained by integrating the noise spectrum in the frequency range of 100 Hz to 1000 Hz. The PSD of 2,6-NDA comes from approximately 30 000 G–t traces collected at 0.1 V and 0.3 V, respectively.

Theoretical models and computational details

Molecular optimization and frequency analysis were performed using the Gaussian 16 package. The single point energies were calculated using the M06-2X functional and 6-311+G(d,p) basis set with the SMD solvation model. Chlorobenzene was used as the solvent. The binding energy under an electric field was obtained by subtracting the energy of the two monomers from the energy of the dimer. The stretched dimer configuration with the maximum binding energy has been used as the initial geometry for structure optimization in the solvent by using the B3LYP-D3 (BJ) functional together with the 6-31(d) basis set. The optimized molecular lengths are shown in Table S3 (ESI†). The electric field is introduced using the keyword "Field = M ± N", with the direction aligned along the molecular backbone. Specifically, for 2,6-NDA and 2,6-NAP, the electric field direction is parallel to the line connecting the two nitrogen atoms. For β-NA and 5,6,7,8-THDA, the electric field direction parallels the line connecting the nitrogen and carbon atoms farthest from it. After obtaining the optimized configurations, the ESP at different electric fields is computed using Gaussian 16 with the same theoretical level. Under zero electric field, the optimized monomer and dimer structures were subsequently sandwiched by two Au (111) electrodes. The "tips" are composed of 4 gold atoms, and the electrode consists of 6 layers of 5 × 5 gold atoms. The molecular junction's electronic structure and transmission functions were calculated using the Siesta package and Tran SIESTA codes. The GGA-PBE functional and double-ζ polarized (DZP) basis were used. The cut off energy was set to 160 Ry. The molecule remains rigid, and the distance between the molecule and the electrode was optimized. The transmission functions were calculated with a 1 × 1 × 100 Monkhorst type k-grid for the electrodes and the Γ point for the device region.

Results and discussion

π–π stacking modulated by electric field

The STM-BJ technique enables forming nanogaps between the gold tip and the gold substrate by precisely controlling the movement of the tip. Within the nanogap, a single-molecule junction could be formed through the two-terminal anchors of the molecules, and the π–π stacked molecular dimer junctions can also be established during the electrode separation process. We firstly employed the simplest naphthalene derivative (2,6-naphthalenediamine, denoted as 2,6-NDA) with a benzene ring backbone and two terminal amino anchoring groups to create a π–π stacking dimer, as shown in Fig. 1a.[17] Fig. 1b delineates the 1D conductance histogram profiles under a small bias voltage (0.1 V). A peak located at 3.3 × 10^{-3} G_0 (254 nS, high conductance denoted as HC) as marked by the arrow can be clearly observed, which can be assigned to the conductance of single 2,6-NDA. Meanwhile, a faint peak at ~6.0 × 10^{-5} G_0 (low conductance, denoted as LC) as marked by the shaded rectangle can be observed. We further collected thousands of

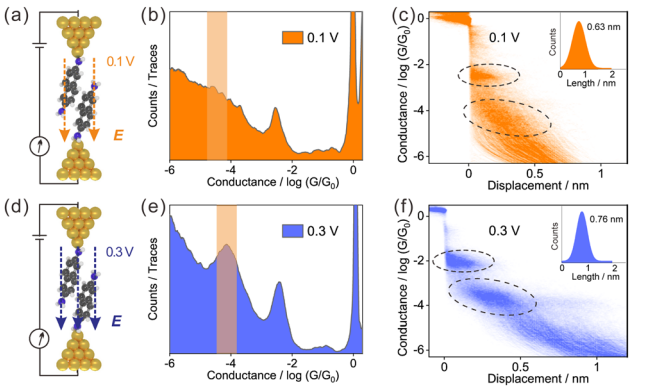

Fig. 1 Conductance measurement of 2,6-NDA molecular junctions performed under different bias voltages. (a) Schematic of the STM-BJ technique featuring a weak π–π stacking with 2,6-NDA. (b) 1D conductance histogram at a bias voltage of 0.1 V. The arrow indicates the position of the HC peak, and the shaded rectangle marks the approximate position of the LC peak. (c) 2D conductance histogram at a bias voltage of 0.1 V. The inset delineates the distribution of the relative stretching distance of the molecular junctions. (d) Schematic diagram of the π–π stacked molecular junction under an increased electric field at a bias voltage of 0.3 V. (e) and (f) The 1D and 2D conductance histogram of the molecular junctions at a bias voltage of 0.3 V.

individual conductance traces and constructed a two-dimensional (2D) conductance histogram, as illustrated in Fig. 1c. It can be found that the slope of the HC plateau remained nearly constant as marked by the dashed ellipse, signifying a consistent conductance. In contrast, the low conductance plateau exhibited a noticeable reduction in slope. Accordingly, we suspect that the LC peak originates from the formation of molecular dimer junctions *via* π–π stacking, since the overlapped area between two π–π stacked molecules will be reduced during the electrode's separation process and thus the conductance of the dimer junction will continuously decrease.

Fig. 1d shows the schematic diagram of the molecular dimer junction when a larger bias voltage is applied. Fig. 1e and f show the corresponding conductance histogram. Interestingly, the intensity of the LC peak in the conductance histogram was greatly enhanced and right-shifted to a high value when the bias voltage increased from 0.1 V to 0.3 V. Meanwhile, the probable length of the conductance plateau increased from 0.63 nm to 0.76 nm. This observation suggests that the LC peak would not originate from the different bond configurations (top, hollow, bridge),[30] since the length of the conductance plateau in different bond configurations for a rigid molecule is typically independent of the bias voltage. Instead, these observations are in line with the conjecture that the LC peak originates from the molecular dimer formed *via* intermolecular π–π coupling, which is enhanced by the electrical field upon a higher bias. We will address this issue in more detail later.

Flicker noise measurement and correlation analysis

To probe the charge transport dynamics across the molecular junctions at the LC state, we performed flicker noise measurement under different bias voltages. The methodologies of flick noise measurement were comprehensively introduced in prior studies.[25,31,32] Here, the top electrode was suspended for 150 ms during the retracting process once the low conductance plateau was observed (conductance range from $10^{-4.2}$ G_0 to $10^{-4.9}$ G_0), and the conductance-time (G–t) traces were recorded during the electrode suspension process. The noise spectra were derived through a fast Fourier transform of each G–t curve, and the noise power was subsequently obtained by integrating the noise spectrum within the frequency range of 100 Hz to 1000 Hz. Fig. 2a and b presents the power spectral density (PSD) of 2,6-NDA derived from approximately 30 000 I–t traces acquired at biases of 0.1 V and 0.3 V, respectively. It can be found that the 'N' value decreases with the increase of the bias voltage. Notably, amino anchored molecules (the π orbital is absent in this anchoring group) are used in this noise measurement, and thus the change of the bonding angle, *i.e.*, the change of weight between through-space and through-bond at the anchoring interface, will not result in a change of "N" value.[25] Therefore, the decrease of the "N" value can be attributed to the enhancement of intermolecular coupling (π–π coupling) upon the increased electric field. More information regarding PSD for a series of molecules can be seen in Fig. S1 (ESI†).

To elucidate the relationship between the two conductance plateaus, we conducted a conductance correlation analysis to discern the relationships between different conductance states.[33,34] A negative correlation coefficient indicates that one conductance state occurs while the other is absent, indicating that the two states cannot coexist. Conversely, a positive correlation coefficient implies that the two conductance states occur in the same conductance trace or are both absent simultaneously. Fig. 2c illustrates the cross-correlation plot of the two conductance states under 0.3 V, showing a positive correlation coefficient. This finding signifies that the LC state originates from the molecular dimer, confirming our earlier conclusion.

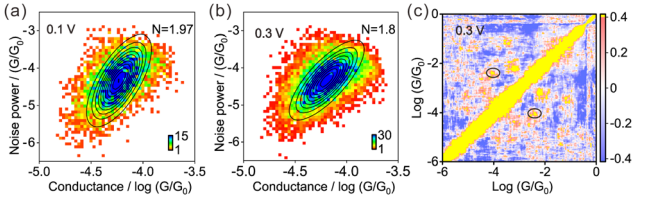

Fig. 2 The flicker noise spectroscopy and conductance correlation analysis of 2,6-NDA molecular junctions. (a) 2D histogram of normalized flicker noise power *versus* average conductance at the LC state under a bias voltage of 0.1 V and (b) under a bias voltage of 0.3 V. (c) Cross-correlation analysis of two conductance states at 0.3 V. The red area represents positive correlation, and the blue area represents negative correlation.

Regulating π–π stacking with different aromatic molecules

To investigate the mechanism of bias-regulated π–π stacking, we conducted further investigations on a series of molecules with different anchoring groups and frameworks. Fig. 3a presents the integrated 1D conductance histograms of 2,6-NDA molecule junctions, illustrating the effect of bias voltage (@ 0.1 V; @ 0.3 V). The corresponding 2D conductance histograms are provided in Fig. S2 (ESI†). Our primary focus is on the LC peak, which likely originates from the molecular dimer junctions. We observed an increase in the intensity of the LC peak and a right

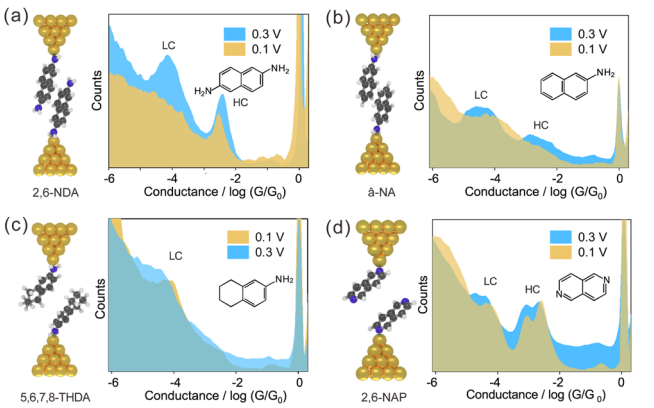

Fig. 3 Conductance histograms of four types of aromatic molecules under different bias voltages. (a)–(d) show the 1D conductance histograms for each type of molecular junction. The left panel displays the corresponding dimer molecular junction. Inset: schematics of the molecule. The conductance measurements for each type of molecule were performed under 0.1 V or 0.3 V. Each histogram is constructed from approximately 3000 individual conductance traces.

shift in its position upon a higher bias voltage. We attribute this observation to the enhanced dimer formation *via* π–π stacking under the higher bias.

It is possible that the low conductance observed stems from molecular dimers formed *via* hydrogen bonds, as molecules with two amino terminals have the capacity to form dimers through hydrogen bonding between neighbouring molecules.[35,36] To exclude this possibility, we performed a control experiment by adding ethanol reagent, which can dissociate the potential intermolecular hydrogen bonds. It is found that the low conductance peak can still be observed, see Fig. S3 (ESI†) for details. To confirm that the dimer formation does not arise from the hydrogen bonds, an experiment was performed using β-naphthylamine (denoted as β-NA) molecules. Unlike 2,6-NDA, the β-NA molecule possesses only a unique amino anchoring group at one end, making it impossible to form a molecular dimer junction *via* intermolecular hydrogen bonding. Nonetheless, both HC and LC peaks were observed in the conductance histogram, as shown in Fig. 3b. The HC peak can be attributed to the β-NA monomer molecular junctions, anchored to one electrode *via* an amino group and coupled to another electrode *via* van der Waals interactions between the benzene ring and the gold electrode.[37,38] Fig. 3b shows that the HC peak becomes obviously visible as the bias voltage increases from 0.1 V to 0.3 V, which can be attributed to the fact that van der Waals interactions between the benzene ring and gold electrode can be enhanced by the bias voltage.[37] Due to the absence of the amino anchoring group at one terminal, the LC peak then can be conclusively assigned to the molecular dimer formed *via* π–π interaction rather than hydrogen bonding. Fig. 3b demonstrates that the intensity of the LC peak increases upon an increased bias voltage, indicating that the bias voltage influences the π-stacking interactions for β-NA molecular junctions.

We further investigated the effect of bias voltage regulation on molecules with different π–π coupling strengths. Fig. 3c presents the conductance histograms of 5,6,7,8-tetrahydronaphthalen-2-amine (denoted as 5,6,7,8-THDA) molecular junctions. In comparison to 2,6-NDA and β-NA, 5,6,7,8-THDA features a cyclohexane end-group, where a cyclohexane ring substitutes one benzene ring, which increases steric hindrance due to the additional hydrogen atoms in cyclohexane, thus suppressing the π–π interactions. Consequently, we anticipated a reduced impact of light and electric fields on the LC peak for this molecule. Fig. 3c validates our prediction that the bias only exerts a weak effect on the LC peak, since the intensity of the LC peak for this molecule almost remains unchanged upon a varied bias.

For comparison, we also investigated molecules with pyridine anchoring groups at both ends (2,6-naphthyridine, denoted as 2,6-NAP). As illustrated in Fig. 3d, the LC peak showed no significant change under the influence of electric fields. This observation can be attributed to an imbalance in electron cloud density within the molecule caused by a lone pair of electrons on the N atom in the pyridine ring. As a result, forming a π–π stacked dimer with strong coupling becomes difficult, leading to the almost unaffected LC peak of 2,6-NAP by electric fields. More experimental results under intermediate bias voltage employing different types of molecules can be seen in Fig. S4 and S5 (ESI†). All the data show that the bias voltage has a strong regulation effect on 2,6-NDA and β-NA but a relatively weak regulation effect on 5,6,7,8-THDA and 2,6-NAP molecular junctions.

Calculation of binding energy, transmission and dipole moment

Fig. 4 shows the binding energy of the four types of molecular dimers as a function of the separation between the two monomers. The binding energy serves as an indicator of the coupling strength between the two monomers. As depicted in Fig. 4a, the 2,6-NDA and β-NA dimers exhibit a larger π–π coupling strength than the one formed by 5,6,7,8-THDA and 2,6-NAP. The decrease of binding energy for 5,6,7,8-THDA is attributed to the hydrogenation of one benzene ring, which causes steric hindrance between two neighbouring molecules. Similarly, the binding energy reduction for 2,6-NAP can be attributed to the mutual repulsion between the nitrogen atoms in the benzene rings.[39,40]

Fig. 4b shows the transmission functions of the four types of dimers with maximum binding energy calculated based on the non-equilibrium Green's function combined with density functional theory (NEGF-DFT), see Fig. S6 and S7 (ESI†) for detailed information. The transmission coefficients of the four types of dimers exhibit a low value at the Fermi level which is proportional to the conductance. Meanwhile, we calculated the transmission of the four types of molecular monomers, see Fig. S8 (ESI†). Compared to the dimer, the corresponding monomer exhibits more than one order of magnitude higher transmission coefficient at the Fermi energy, which is consistent with the experimental observation.

Since planar-already molecules that are not likely to undergo significant geometrical changes were used in our experiment, we tend to believe that a more universal mechanism plays an

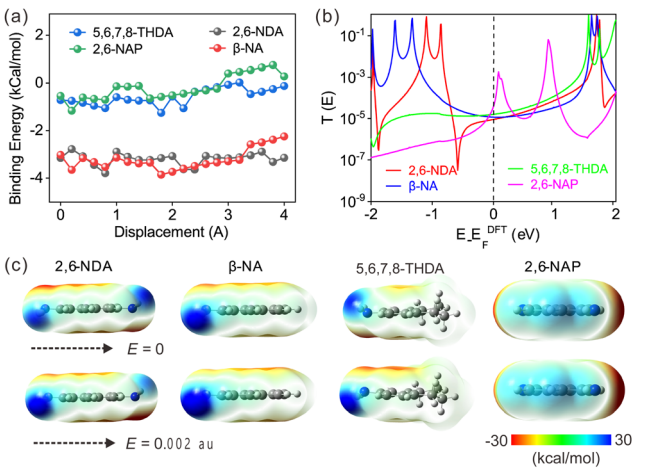

Fig. 4 Theoretical calculations of binding energy, transmission function, and electrostatic potential. (a) Binding energy of the dimers as a function of stretching distance. (b) Calculated transmission coefficient for four dimer junctions. (c) The electrostatic potential of four types of monomers under zero and 0.002 au electric field (1 au = 514 V nm^{-1}).

active role in the observation of π–π interaction influenced by the bias voltage:[22,41] (1) The applied voltage, which could create a strong electric field up to 5×10^8 V m^{-1}, will affect the molecular dipole moment, thereby influencing the π–π interaction *via* electrostatic attraction.[22] (2) The bias voltage also affects the alignment of molecules. When exposed to an electric field, the molecules inside the gap gradually align with the field direction in an orderly fashion, thereby enhancing the π–π stacking between molecules.[22,41] Therefore, these results indicate that the dipole moments of molecules play a more important role than the order alignment in regulating the intermolecular interaction.

To this end, we calculated the dipole moment of each monomer and dimer under different electric fields, see Table S1 and Fig. S9 (ESI†) for details. The dipole moment of 2,6-NDA, which is zero when no electric field is applied, exhibits the most significant change under the applied electric field. To further explore how the dipole moment changes upon the electric field, we plotted the electrostatic potential (ESP) distribution of four molecules under different electric fields, as shown in Fig. 4c. By closely examining the ESP of 2,6-NDA and β-NA, it is evident that the electric field significantly influences the ESP distribution around the amino groups (electron-donating group), and the degree of the influence on the right and left amino groups is different. Under a zero electric field, the ESP distribution around the amino groups on both sides is centrally symmetric, resulting in zero net dipole moment. When an electric field is applied, the overall ESP distribution of the molecule becomes asymmetric, generating a dipole moment along the direction of the external electric field.[42] In contrast, β-NA has only one amino group, and thus the overall change in the dipole moment of β-NA is smaller than that of 2,6-NDA. It is essential to emphasize that a molecular dimer formation results from a combined influence of the dipole moment and the intermolecular coupling strength. For molecules 5,6,7,8-THDA and 2,6-NAP, the steric hindrance between their monomers results in the weakened impact of the electric field; see Tables S2 (ESI†) for more details. Additionally, natural bond orbital analysis was performed to address the effect of the lone pairs of nitrogen on π–π stacking,[15] and the calculated results supported our claim, see Fig. S10 and Table S4, S5 for details ESI.†

Conclusions

In summary, we investigate the intermolecular π–π interaction of a series of molecules with rigid backbones and varied anchoring groups by performing conductance measurements with thousands of single molecular junctions. Interestingly, it was found that upon a higher bias voltage, the LC peak of the molecular junction shifts to a higher value and the intensity of the LC peak increased significantly, implying that the π–π coupling between the rigid aromatic molecules is greatly enhanced. Supported by the calculation based on the NEGF-DFT calculations, we uncovered that the enhancement of π–π interaction under an electric field is caused by the alteration of molecular dipole moments rather than the changes of the molecular conformation upon a higher bias voltage. These findings not only promote the understanding of the structure-conductance relationship of aromatic molecular dimers at the single molecule level, but also provide non-destructive approaches to regulate the intermolecular interaction, which is crucial for designing new functional materials, assembling stable biomolecules, and realizing novel single molecule-based devices.

Conflicts of interest

There is no conflict of interest to report.

Acknowledgements

We acknowledge the financial support from the National Key R&D Program of China (2021YFA1200103), the National Natural Science Foundation of China (22273041, 91950116, 11804170, 12174201, 21973081), and the Natural Science Foundation of Tianjin (19JCZDJC31000, 19JCJQJC60900, 22JCYBJC01310). The authors are thankful for the help of X-Tech with the STM-BJ setup.

References

1 C. R. Martinez and B. L. Iverson, *Chem. Sci.*, 2012, **3**, 2191–2201.
2 S. Wang, J. Xu, W. Wang, G.-J. N. Wang, R. Rastak and F. Molina-Lopez, *et al.*, *Nature*, 2018, **555**, 83–88.
3 S. Dong, H. Zhang, L. Yang, M. Bai, Y. Yao and H. Chen, *et al.*, *Adv. Mater.*, 2012, **24**, 5576–5580.
4 H. H. Ge, Y. Qiu, Z. W. Yi, R. Y. Zeng and G. Y. Zhang, *Int. J. Biol. Macromol.*, 2019, **124**, 895–902.
5 J.-H. Deng, J. Luo, Y.-L. Mao, S. Lai, Y.-N. Gong and D.-C. Zhong, *et al.*, *Sci. Adv.*, 2020, **6**, eaax9976.
6 M. Zaccheddu, C. Filippi and F. Buda, *J. Phys. Chem. A*, 2008, **112**, 1627–1632.
7 D. Fujita, Y. Ueda, S. Sato, N. Mizuno, T. Kumasaka and M. Fujita, *Nature*, 2016, **540**, 563–566.
8 S. Biswas, S. Sen, J. Im, S. Biswas, P. Krstic and B. Ashcroft, *et al.*, *ACS Nano*, 2016, **10**, 11304–11316.
9 C. Wang, H. Dong, W. Hu, Y. Liu and D. Zhu, *Chem. Rev.*, 2012, **112**, 2208–2267.
10 C. Wang, H. Dong, L. Jiang and W. Hu, *Chem. Soc. Rev.*, 2018, **47**, 422–500.
11 H. Xu, G. He, S. Chen, S. Chen, R. Qiao and H. Luo, *et al.*, *Macromolecules*, 2021, **54**, 8195–8206.
12 W. Zheng, J. Liu, Y. Guo, G. Han and Y. Yi, *Adv. Funct. Mater.*, 2022, **32**, 2108551.
13 M. R. Tuttle, S. T. Davis and S. Zhang, *ACS Energy Lett.*, 2021, **6**, 643–649.
14 Y. Li, L. Wang, X. Gao, Y. Xue, B. Zhan and X. Zhu, *J. Mater. Chem. A*, 2024, **12**, 7807–7816.

15 S. Sao, S. Naskar, N. Mukhopadhyay, M. Das and D. Chaudhuri, *Chem. Commun.*, 2018, **54**, 12186–12189.
16 R. Frisenda, V. A. Janssen, F. C. Grozema, H. S. Van Der Zant and N. Renaud, *Nat. Chem.*, 2016, **8**, 1099–1104.
17 S. Wu, M. T. González, R. Huber, S. Grunder, M. Mayor and C. Schönenberger, *et al.*, *Nat. Nanotechnol.*, 2008, **3**, 569–574.
18 S. A. Lee, S. Hotta and F. Nakanishi, *J. Phys. Chem. A*, 2000, **104**, 1827–1833.
19 A. Magyarkuti, O. Adak, A. Halbritter and L. Venkataraman, *Nanoscale*, 2018, **10**, 3362–3368.
20 D. Stefani, K. J. Weiland, M. Skripnik, C. Hsu, M. L. Perrin and M. Mayor, *et al.*, *Nano Lett.*, 2018, **18**, 5981–5988.
21 P. Zhou, Y. Fu, M. Wang, R. Qiu, Y. Wang and J. F. Stoddart, *et al.*, *J. Am. Chem. Soc.*, 2023, **145**, 18800–18811.
22 C. Zhang, J. Cheng, Q. Wu, S. Hou, S. Feng and B. Jiang, *et al.*, *J. Am. Chem. Soc.*, 2023, **145**, 1617–1630.
23 X. Li, Q. Wu, J. Bai, S. Hou, W. Jiang and C. Tang, *et al.*, *Angew. Chem., Int. Ed.*, 2020, **59**, 3280–3286.
24 Y. Tang, Y. Zhou, D. Zhou, Y. Chen, Z. Xiao and J. Shi, *et al.*, *J. Am. Chem. Soc.*, 2020, **142**, 19101–19109.
25 W. Zhang, Z. Zhao, M. Tan, A. Adijiang, S. Zhong and X. Xu, *et al.*, *Chem. Sci.*, 2023, **14**, 11456–11465.
26 S. Zhang, C. Guo, L. Ni, K. M. Hans, W. Zhang and S. Peng, *et al.*, *Nano Today*, 2021, **39**, 101226.
27 X. Zhao, Y. Yan, M. Tan, S. Zhang, X. Xu and Z. Zhao, *et al.*, *SmartMat*, 2024, e1280.
28 H. Ju, J. Wang, W. Liu, J. Hao, M. Li and Y. Xu, *et al.*, *CCS Chem.*, 2024, 1–20.
29 M. Tan, F. Sun, X. Zhao, Z. Zhao, S. Zhang and X. Xu, *et al.*, *J. Am. Chem. Soc.*, 2024, **146**, 6856–6865.
30 J. Dalmieda, W. Shi, L. Li and L. Venkataraman, *Nano Lett.*, 2024, **24**, 703–707.
31 O. Adak, E. Rosenthal, J. Meisner, E. F. Andrade, A. N. Pasupathy and C. Nuckolls, *et al.*, *Nano Lett.*, 2015, **15**, 4143–4149.
32 M. H. Garner, H. Li, Y. Chen, T. A. Su, Z. Shangguan and D. W. Paley, *et al.*, *Nature*, 2018, **558**, 415–419.
33 A. Halbritter, P. Makk, S. Mackowiak, S. Csonka, M. Wawrzyniak and J. Martinek, *Phys. Rev. Lett.*, 2010, **105**, 266805.
34 P. Makk, D. Tomaszewski, J. Martinek, Z. Balogh, S. Csonka and M. Wawrzyniak, *et al.*, *ACS Nano*, 2012, **6**, 3411–3423.
35 S. Mukherjee, S. Majumdar and D. Bhattacharyya, *J. Phys. Chem. B*, 2005, **109**, 10484–10492.
36 N. C. Seeman and H. F. Sleiman, *Nat. Rev. Mater.*, 2017, **3**, 17068.
37 Y. Wei, L. Li, J. E. Greenwald and L. Venkataraman, *Nano Lett.*, 2023, **23**, 567–572.
38 S. Kaneko, T. Nakazumi and M. Kiguchi, *J. Phys. Chem. Lett.*, 2010, **1**, 3520–3523.
39 A. Banerjee, A. Saha and B. K. Saha, *Cryst. Growth Des.*, 2019, **19**, 2245–2252.
40 E. G. Hohenstein and C. D. Sherrill, *J. Phys. Chem. A*, 2009, **113**, 878–886.
41 S. Tanimoto, M. Tsutsui, K. Yokota and M. Taniguchi, *Nanoscale Horiz.*, 2016, **1**, 399–406.
42 S. Tao, L.-J. Yu, R. Pang, Y.-F. Huang, D.-Y. Wu and Z.-Q. Tian, *J. Phys. Chem. C*, 2013, **117**, 18891–18903.

